Supporting Information

Molecular Engineering of an Ether-Nitrile Constructs Robust Dual-interphases for Ultra-Stable 4.5 V Lithium Metal Batteries

Experiments

Materials preparation:

The 1,2-Bis(2-methoxyethoxy)ethane (TGDME, 99.5%) and 1,1,2,2-trifluoroethyl-2,2,3,3-tetrafluoropropyl ether (TTE, 99.5%) were all purchased from Shanghai Aladdin Biochemical Technology Co., Ltd. The Battery-grade (99.9%) lithium bis(fluorosulfonyl)imide (LiFSI) was purchased from DoDoChem. The commercial EC-based electrolyte (ECE, 1 M $LiPF_6$ in EC/EMC=1:1 by vol.) was bought from Shenzhen Capchem Technology Co, Ltd. All reagents were stored in the Ar-filled glove box (water and oxygen contents < 0.1 ppm) immediately upon receipt and used directly to prepare the electrolytes. The concentrations of GT, GBT and GMT were 2 M (local = 5 M) shown in **Table S1** and stored for no more than two weeks to prevent denaturation. The M stands for 1 mole of salt dissolved in 1 liter of solvent.

$LiMn_{0.8}Fe_{0.2}PO_4$ (LM8F2P) was synthesized using a modified solid-state method as described elsewhere.[1] Chemicals of LiH_2PO_4, $MnC_4H_6O_4 \cdot 4H_2O$, $FeC_2O_4 \cdot 2H_2O$ and $H_2C_2O_4 \cdot 2H_2O$ with the molar ratio of 1:0.8:0.2:1 were fully ball-milled with sucrose (the molar ratio of sucrose to $MnC_4H_6O_4 \cdot 4H_2O$ was about 0.602) for 6 h, and then the milled mixture was dried and then heated at 700 ^oC for 15 h under an Ar atmosphere (heating rate: 5 ^oC min^{-1}). The $LiMn_{0.8}Fe_{0.2}PO_4$ composition strikes an optimal balance between high energy density and long-term cycling stability. The LMFP cathode (3.4 mg cm^{-2}), high-loading LMFP cathode (≥ 19.5 mg cm^{-2}) were fabricated by coating a slurry containing LMFP particles, conductive carbon, PVDF binder, and NMP solvent onto the carbon-coated aluminum foil. Li metal sheet (250 μm) were obtained from Guangdong Canrd New Energy Technology Co,. Ltd. and the diameters of the Li-metal disk and the cathode disk are 15.6 mm and 14.0 mm, respectively. The Li@Cu electrode sheet was prepared by depositing Li on Cu foil[2], and the amount of Li is controlled by N/P as 2 according to the loading capacity (i.e., P) of the high-load LMFP cathode (19.5 mg/cm^2).

Cells assembling:

The Li||LMFP cells with Li anode were constructed within a glove box, utilizing CR2025-type cells and 40 μL of electrolyte. The assembly process followed a specific sequence: cathode case, cathode, electrolyte, Celgard PE separator (19 mm), anode, nickel foam (16 mm), and anode shell. Additionally, placing a sheet of Al foil between the cathode case and cathode is essential to prevent corrosion of the stainless steel case when exposed to high voltages. For Li@Cu||LMFP cells, a high-loading LMFP cathode, a Li-deposited copper (Cu) anode, and 3g Ah^{-1} of electrolyte were utilized.

Electrochemical tests:

All electrochemical data reported in this study are based on replicate experiments using at least three independent cells. The Galvanostatic Charge and Discharge tests were carried out on the Neware battery test system and the temperature was controlled at 30 ^{o}C. The Li||LMFP and Li@Cu||high-loading LMFP full cells were cycled two times at a current density of 0.1 C for the active process and a current density of 0.5 C was employed for the cycling tests within the voltage range of 3.0-4.5 V.

The long-term charge/discharge tests of Li||Li symmetric cells were cycled at a current density of 0.5 mA cm^{-2} and a capacity of 1 mAh cm^{-2}. And the rate performance of Li||Li cells in different electrolytes was evaluated in a current density range of 0.5 to 4.0 mA cm^{-2}. The modified Aurbach method was also used to evaluate the reversibility of the studied electrolytes.[3] Initially, a single Li deposition/stripping cycle at a high capacity (5 mAh/cm^2) was executed to precondition the Cu foil and mitigate substrate impact on the test outcomes. Subsequently, a specific capacity (Q_T, 5 mAh cm^{-2}) was deposited on the Cu foil, acting as a lithium reservoir. Throughout both processes, the current density was maintained at 0.5 mA cm^{-2}. Following this, charge/discharge procedures were carried out at 0.5 mA cm^{-2} and 1.0 mAh cm^{-2}(Q_C) for n cycles. Ultimately, an exhaustive strip of the remaining Li reservoir (Q_S) was conducted, reaching a cut-off voltage of 1.0 V, all under a current density of 0.5 mA/cm^2.

The average Coulombic Efficiency (CE_{avg}) o across n cycles is determined using the following equation (**Equation S1**).

$$CE_{avg} = \frac{nQ_c + Q_s}{nQ_c + Q_T} \tag{S1}$$

Q_c represents the deposition capacity over n cycles, consistently set at 1.0 mAh/cm^2. Q_T signifies the initial Li reservoir deposition, while Q_s denotes the capacity stripped from the Cu foil at the conclusion of the process.

For the LSV tests, the Super-P was employed for the working electrode, and the Li sheet as the counter and reference electrode. The executed scan rate and applied voltage scope are 0.1 mV/s and 3.0 to 5.0 V (vs. Li/Li^+), respectively. Tafel plots were measured at a voltage range from -0.15 to 0.15 V (vs. Li/Li^+) in Li||Li cells with a scan rate of 1 mV/s.

The Electrochemical Impedance Spectroscopy (EIS) was measured from 100 kHz to 0.01 Hz and the voltage amplitude was 5 mV. All the tests mentioned above were executed by the electrochemical workstation (Solartron, PAR-Amerek, America).

Characterization:

The Nuclear Magnetic Resonance (NMR) spectrometer was used by JEOL ECZ600R in this work, and each test was performed by dissolving the 50 μL sample in the deuterated chloroform. Raman spectra were obtained using a LabRAN HR spectrometer with a 532 nm wavelength. The morphology and structure of lithium deposition on Cu foil at various temperatures and the cycled NCM523 cathode were analyzed using the Scanning Electron Microscope (SEM, Hitachi SU-8010) and Transmission Electron Microscopy (JEOL2100f). Chemical composition analysis of the electrode/electrolyte interface was conducted using X-ray Photoelectron Spectroscopy (XPS, ESCALAB 250Xi). Sample preparation for SEM and XPS involved conducting the procedures inside a glovebox and transferring the samples into a vacuum-sealed container to prevent exposure to air during transfer. Transition metal dissolution from cycled NCM523 cathodes was confirmed using an inductively coupled plasma-atomic emission spectrometer (ICP-AES, Perkin Elmer Avio200). Separators obtained from cells after 100 cycles with different electrolytes were immersed in 25 ml of 5 wt% HNO_3 for further analysis.

Theoretical calculation:

DFT Calculations. Density functional theory (DFT) calculations were carried out using the vienna ab initio simulation package (VASP)[4] to investigate the absorption energy of different solvent component on the (010) of lithium ferric manganese phosphate (LMFP). The generalized gradient approximation (GGA) with the Perdew–Burke–Ernzerhof (PBE)[5-6] functional was employed, along with DFT+D3 corrections for van der Waals interactions and a Hubbard

U value of 3.29 eV for iron to account for localized 3d electron correlations. Calculations utilized a plane-wave basis set with a 400 eV energy cutoff, a self-consistent field tolerance of 1×10^{-8} eV, and a force convergence criterion of 0.01 eV Å^{-1}. The vacuum slab models featured a 15 Å vacuum along the c axis, with a 2×2×1 Monkhorst–Pack mesh for Brillouin zone sampling.

Molecular dynamics and interaction energy. The molecular structure is positioned at the minimum potential energy surface with no virtual frequency and is optimized by Gaussian 16[7] process utilizing the B3LYP exchange of mixed density functional theory to approximate the 6-311++G (d,p) basis set [8, 9]. The LigparGen program generates the general OPLS-AA force field parameters of solvent molecules, while the GROMACS program is used to perform the molecular dynamics simulation (MD) under three-period boundary conditions [10]. Furthermore, the Li^+ and FSI^- position values were taken from the literature that was previously reported by other researchers [11, 12]. Furthermore, initial atomic coordinate files for MD simulations were created using the Packing Optimization for MD Simulations (PACKMOL) tool, making sure that there was no substantial overlap between molecules and that the simulation system's initial setup was efficiently populated. A conjugate gradient energy minimization approach with a convergence criterion of 1.0 × 10^{-8} is used to solve the initial configuration in order to reduce the number of unrealistic possibilities in the initial structure. To guarantee system equilibration, an MD simulation lasting 10 ns was first run with the NPT ensemble. For additional structural and dynamic analysis, an atomistic simulation lasting 10 ns was then carried out in the isothermal-isobaric (NPT) ensemble, with simulated trajectories collected at 100 fs intervals. Analysis of the electrolyte structure visualization was conducted by VMD and VESTA [13, 14]. The Multiwfn program served as the basis for the molecular orbital analysis, and Equation S1 was used to compute the oxidation potential (E_{ox}) vs. Li/Li$^+$ [15–17].

$$E_{\mathrm{ox}} = \frac{G\left(M^{+}\right) - G\left(M\right)}{F} - 1.4\,V \tag{S2}$$

Each solvation structure's structure is optimized at the B3LYP-D3/TZVP level of theory, and vibrational analysis is carried out to determine the thermal correction to Gibbs Free Energy and make sure local minima are reached. Additionally, the B2PLYP/def2-TZVP level of theory is used to compute the single point energy based on the optimized structure. Assuming a solvation structure with the formula LiAxBy, where x/y is the molecular number of each type of solvent and A and B are the solvent components around a Li^+. Equation S2 is used to compute the de-solvation free energy of LiA_xB_y.

$$\Delta G_{\mathrm{de-solvation}}\left(LiA_xB_y\right)=G_{\mathrm{gas}}\left(Li^+\right)+\mathrm{x}G_{\mathrm{solvent}}\left(A\right)+\mathrm{y}G_{\mathrm{solvent}}\left(B\right)-G_{\mathrm{solvent}}\left(LiA_xB_y\right) \quad \text{(S3)}$$

Where Ggas and Gsolvent denote the gibbs free energy of a species in gas state and solvation state, respectively. For the same structure, the difference between Gsolvent and Ggas is the solvation free energy, which is obtained by subtracting the electronic energy calculated at M052X/6-31G* with SMD solvent model from that calculated without solvent model.

Table S1. Molecular structures and physical information of solvents.


Ethylene Carbonate (EC)

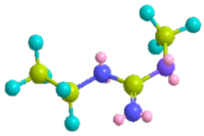
Ethyl Methyl Carbonate (EMC)

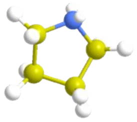
Tetrahydrofuran (THF)

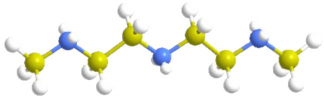
Diethylene Glycol Dimethyl Ether (DGDME)

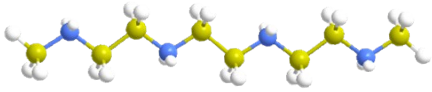
1,2-Bis(2-methoxyethoxy)ethane (TGDME)

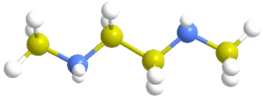
1,2-Dimethoxyethane (DME)


1,1,2,2-Tetrafluoroethyl-2,2,3,3-tetrafluoropropylether (TTE)

Solvents	**Density (g/mL, 20 °C)**	**FP (°C)**	**MP (°C)**	**DC (c/v.m)**	**BP (°C)**	**Viscosity (mPa·S, 20 °C)**
EC	1.41	157	39	85.1	248	1.9
EMC	1.01	23	-55	2.9	109	0.65
THF	0.889	-17	-108.5	7.6	66	0.55
DME	0.87	-2	-58	7.2	83	1.1
DGDME	0.914	67	-68	7.4	162	2.0
TGDME	**0.986**	**118.3**	**-45**	**7.8**	**216**	**3.8**
TTE	**1.53**	**27.5**	**-94.27**	**- -**	**93.2**	**1.43**

FP: flash(ing) point, MP: Melting point, DC: dielectric constant, BP: boiling point.

Table S2. Detailed information of the related electrolytes (M stands for molar·L^{-1}).

Electrolyte	Abbreviation	Composition (Molar ratio)	Concentration
TGDME-based diluted high concentration electrolyte	GT	LiFSI-0.61TGDME-1.98TTE	~ 2.0 M in whole, ~5 M in local
TGDME-based diluted high concentration electrolyte with 1wt% BUN additive	GBT	LiFSI-0.61TGDME-0.11BUN-1.98TTE	~ 2.0 M in whole, ~5 M in local
TGDME-based diluted high concentration electrolyte with 1wt% MPN additive	GMT	LiFSI-0.61TGDME-0.09BUN-1.98TTE	~ 2.0 M in whole, ~5 M in local
EC-based commercial electrolyte	ECE	$LiPF_6$-7.5EC-4.8EMC	1.0 M

BUN: Butyronitrile, C_4H_7N 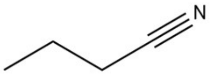 ;

MPN: 3-Methoxypropionitrile, C_4H_7NO 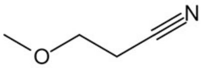 .

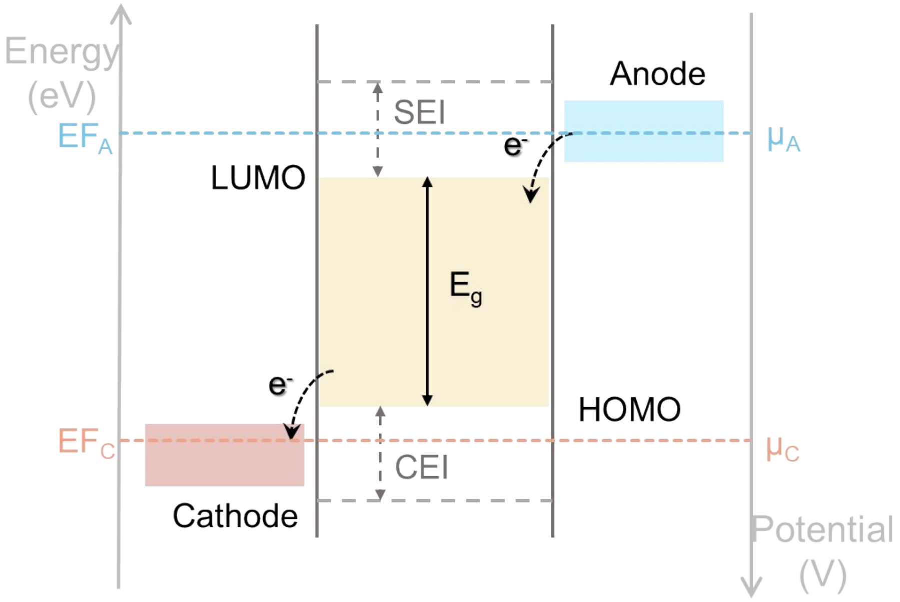

Figure S1. Electron energy levels and electrode potential (μ_A and μ_C) correlated with the Frontier molecular orbital energies (LUMO/HOMO) levels of the electrolyte governing thermodynamic stability, and the enhanced stability by the SEI and CEI formed on anode and cathode.

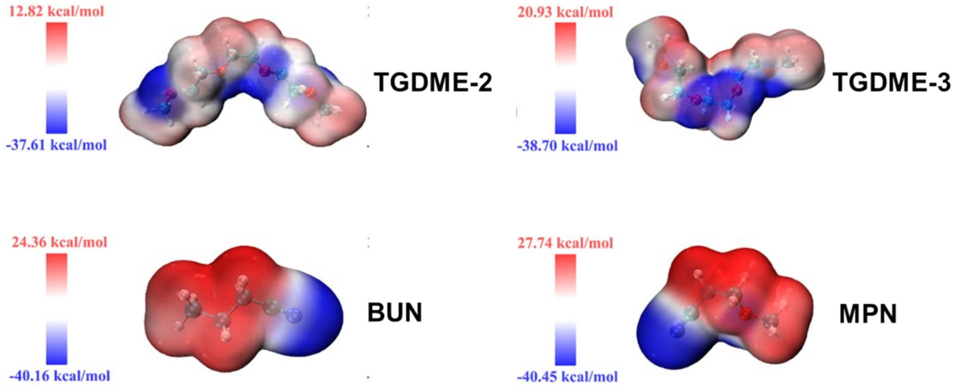

Figure S2. Electrostatic potential of TGDME, BUN and MPN molecules obtained from DFT calculations.

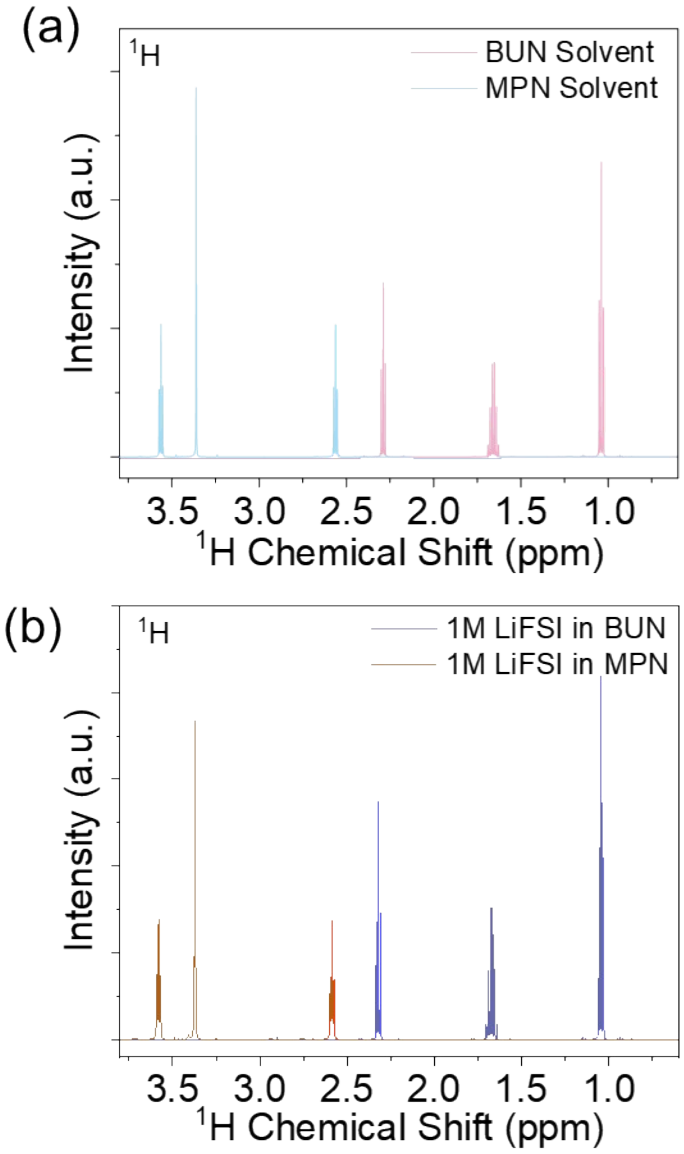

Figure S3. ^{1}H NMR spectra of various solvents and electrolytes.

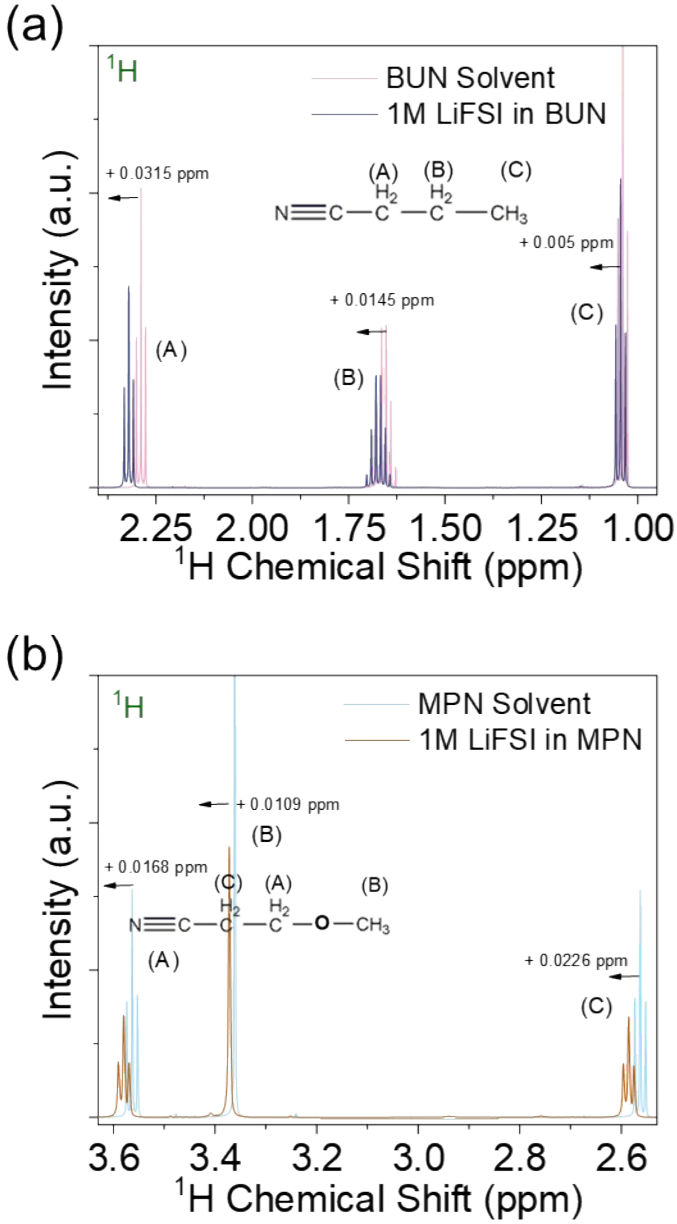

Figure S4. ^{1}H NMR spectra of various solvents and electrolytes.

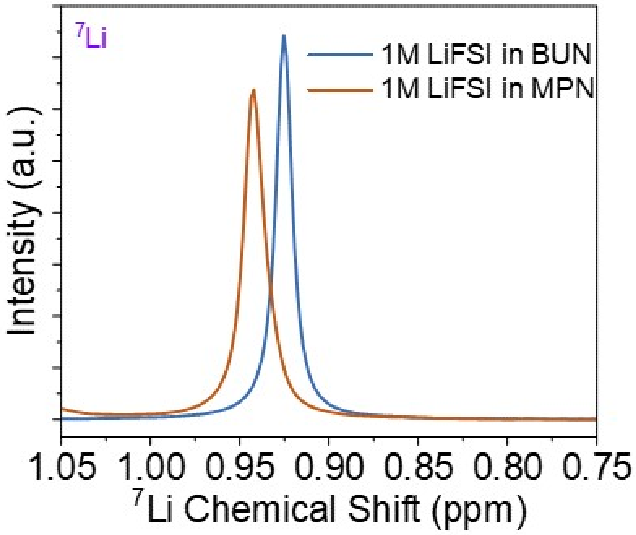

Figure S5. ^{7}Li NMR spectra of electrolytes in different solvents.

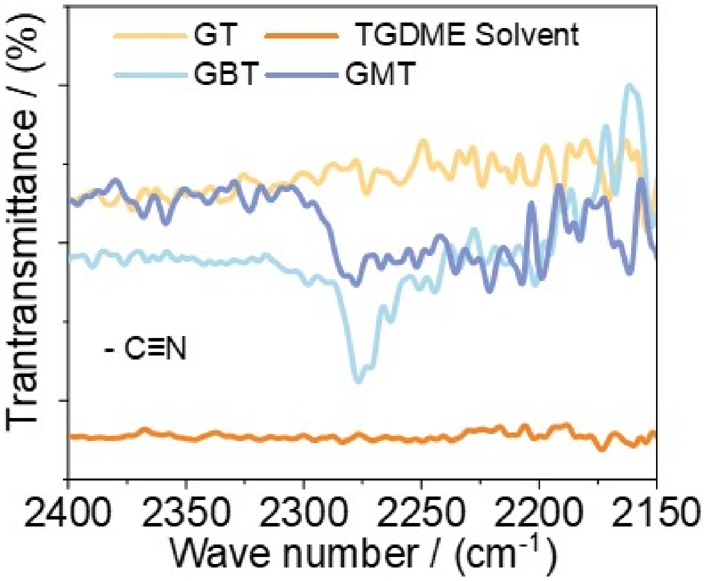

Figure S6. FT-IR spectra of -C≡N stretching vibration band for different electrolytes.

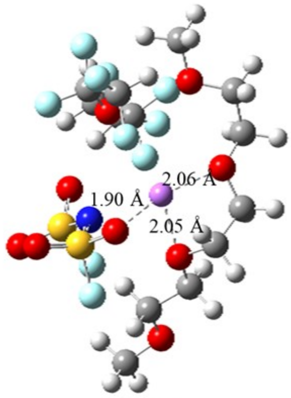

GT

$\triangle G_{\text{de-solvention}}$=321.8174856 KJ·mol^{-1}

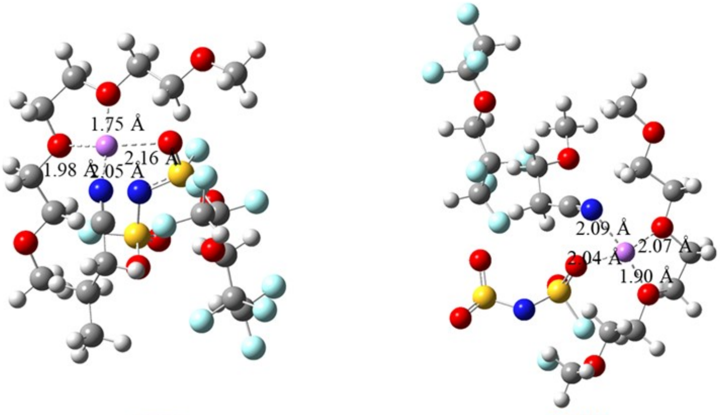

GBT

$\triangle G_{\text{de-solvention}}$=409.1862491 KJ·mol^{-1}

GMT

$\triangle G_{\text{de-solvention}}$=331.6709871 KJ·mol^{-1}

Figure S7. Comparative analysis of Li$^+$ de-solvation energies for solvent/anion species across electrolyte systems.

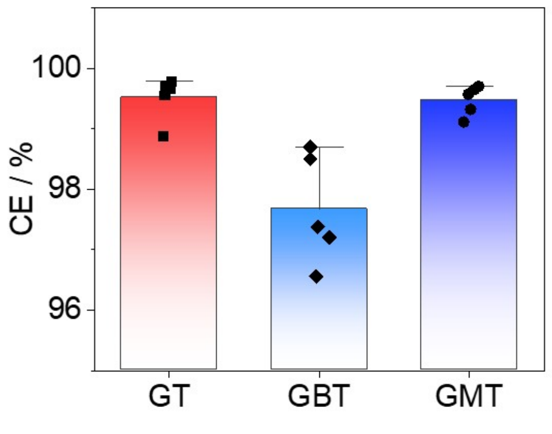

Figure S8. Coulombic efficiency of Li plating/stripping in a Li||Cu cell (error bars represent standard deviation, n=5).

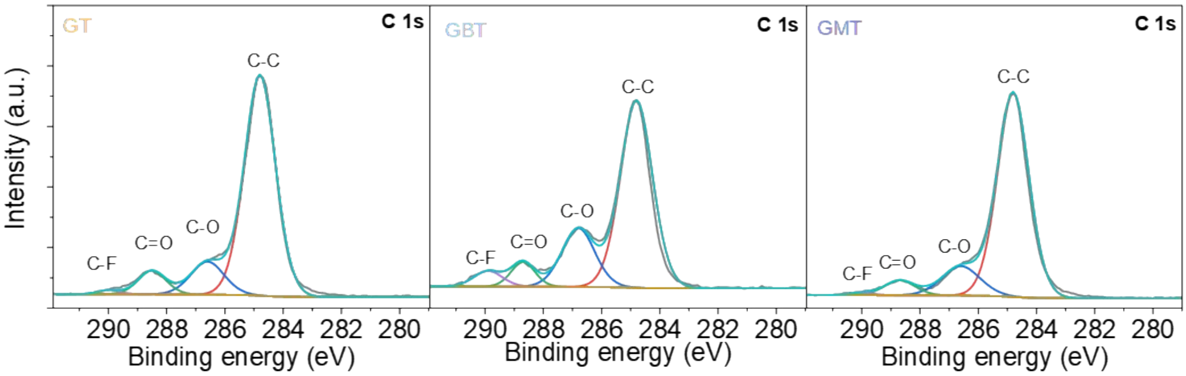

Figure S9. C1s spectra of XPS sputtering on the surface of Li deposited on Cu foil using GT, GBT and GMT, respectively.

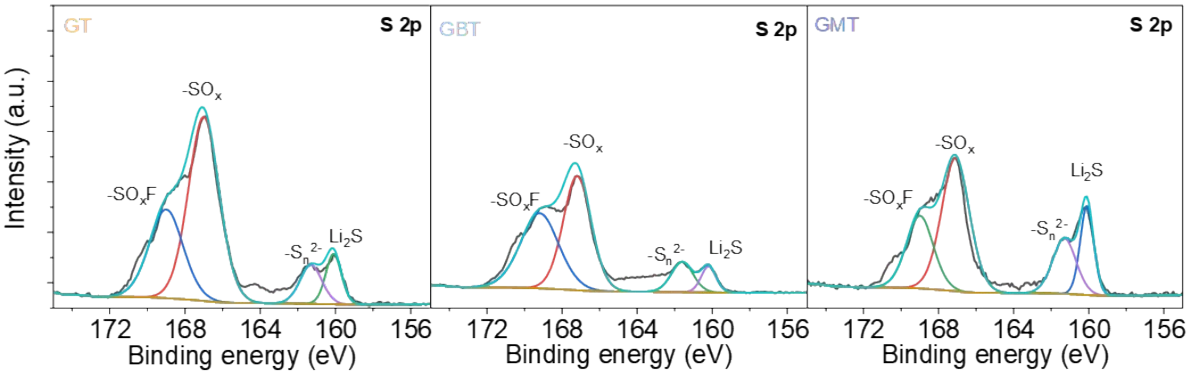

Figure S10. S2p spectra of XPS sputtering on the surface of Li deposited on Cu foil using GT, GBT and GMT, respectively.

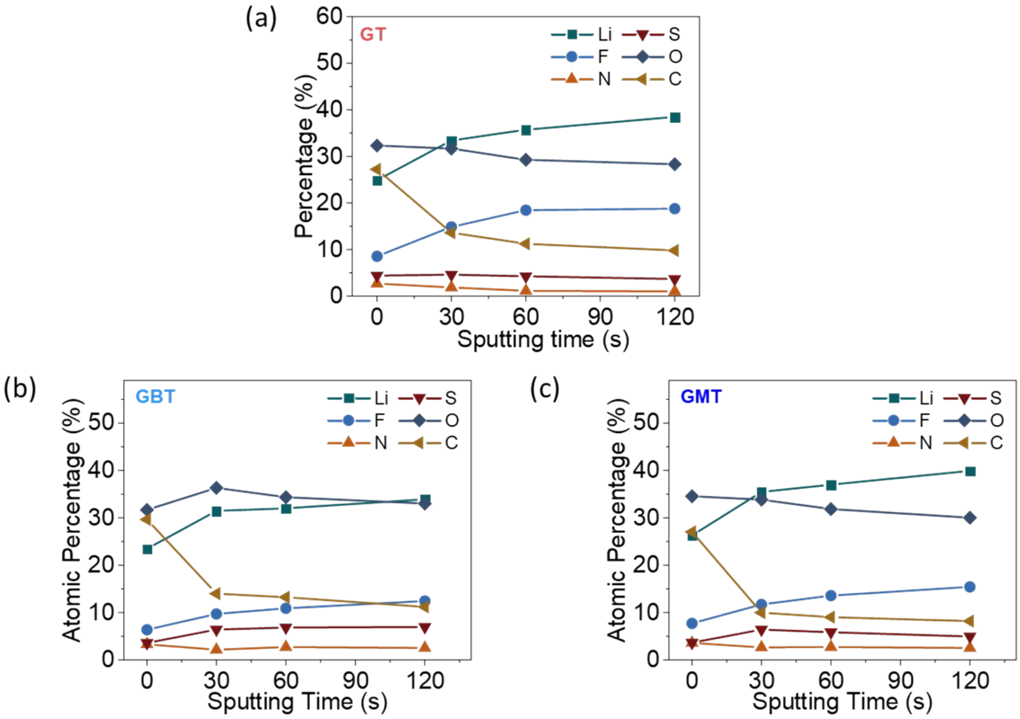

Figure S11. Quantified atomic ratios of the elements within the SEI determined through XPS depth profiling.

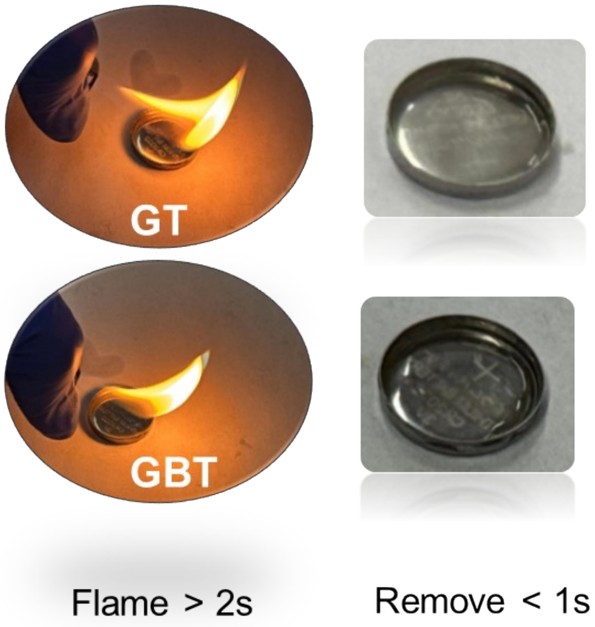

Figure S12. Flame retardancy testing of GT and GBT electrolyte.

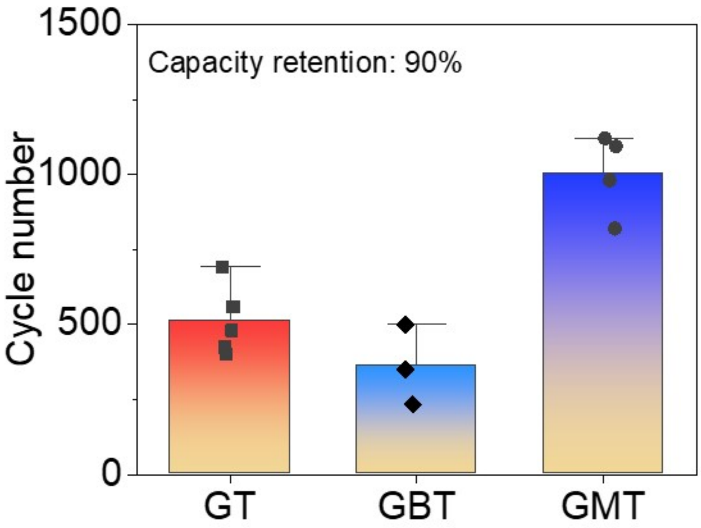

Figure S13. Cycle number at 90% capacity retention in the Li||LMFP cell (error bars represent standard deviation, n ≥ 3).

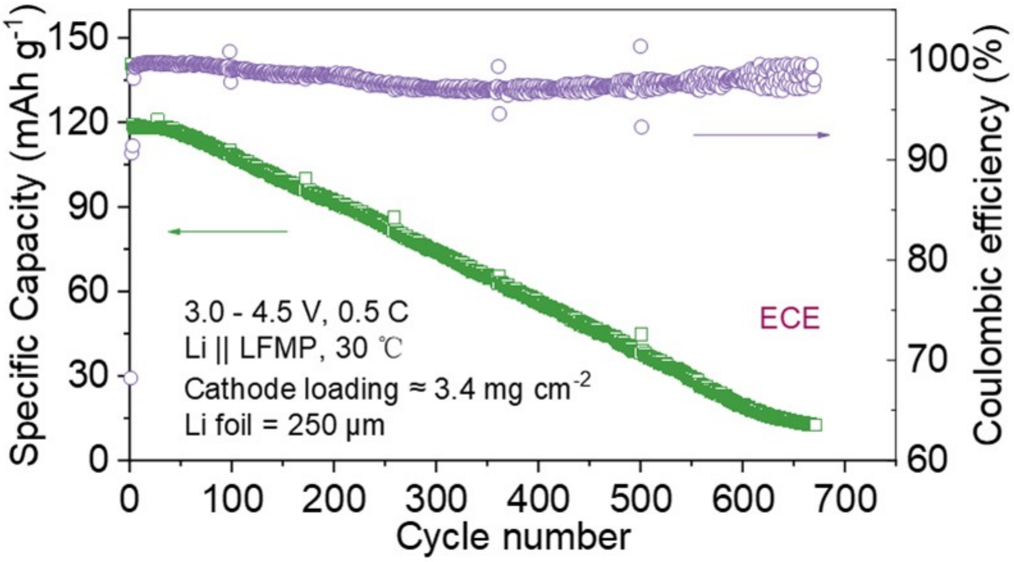

Figure S14. Cycle stability and CE values of Li||LMFP cells using ECE electrolyte in the voltage window of 3–4.5 V.

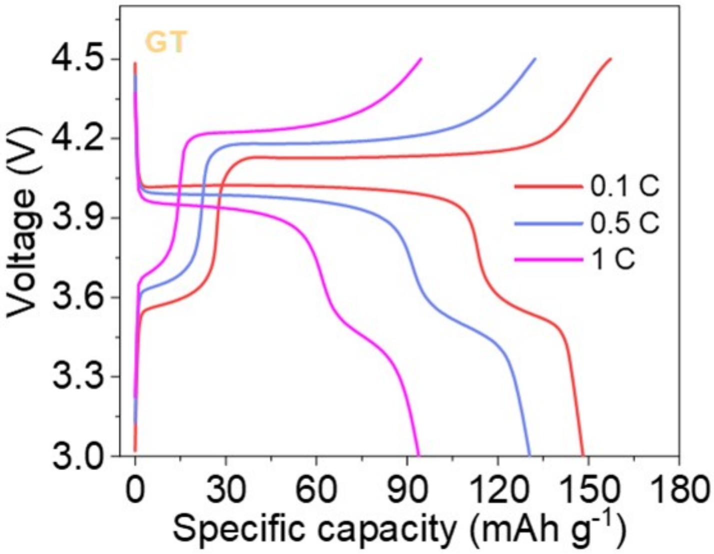

Figure S15. Rate performances of Li||LMFP cells using GT electrolyte in the voltage window of 3–4.5 V.

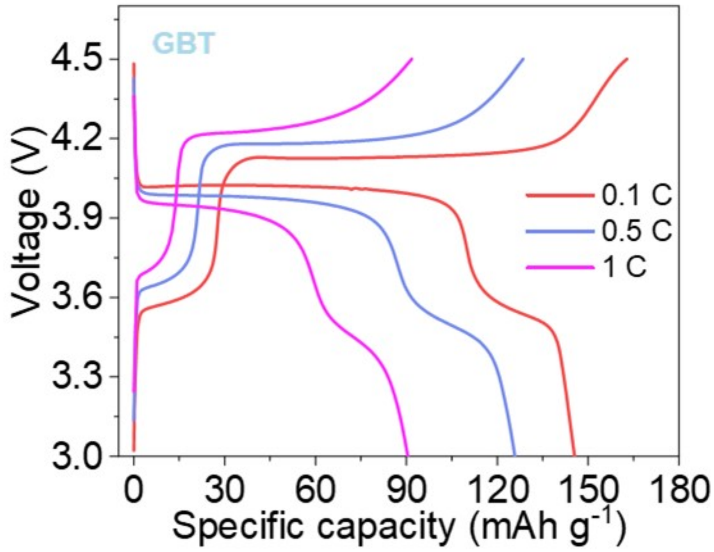

Figure S16. Rate performances of Li||LMFP cells using GBT electrolyte in the voltage window of 3–4.5 V.

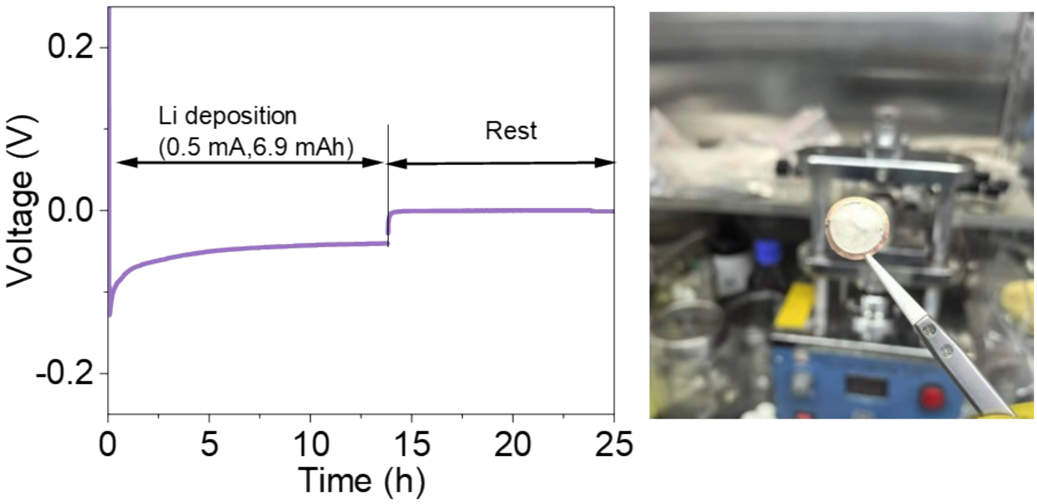

Figure S17. The prepared Li@Cu electrode sheets using different electrolytes and its corresponding voltage-time curve.

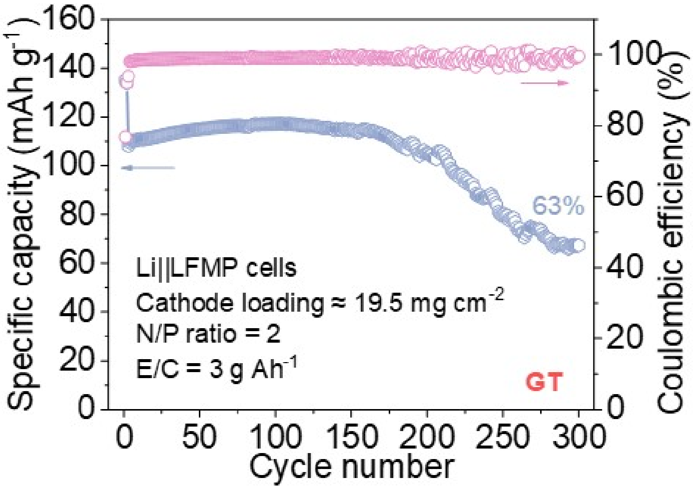

Figure S18. Cycling performances of Li|| LMFP cells using GT electrolyte with a high N/P ratio of 2 at 0.5/0.5C in the voltage window of 3–4.5 V.

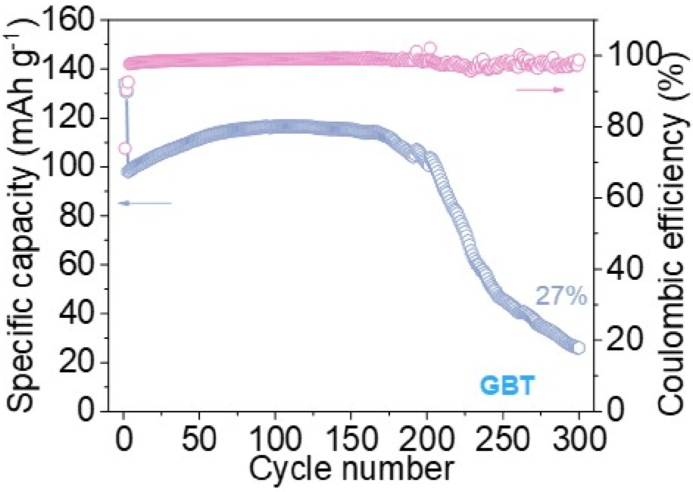

Figure S19. Cycling performances of Li|| LMFP cells using GBT electrolyte with a high N/P ratio of 2 at 0.5/0.5C in the voltage window of 3–4.5 V.

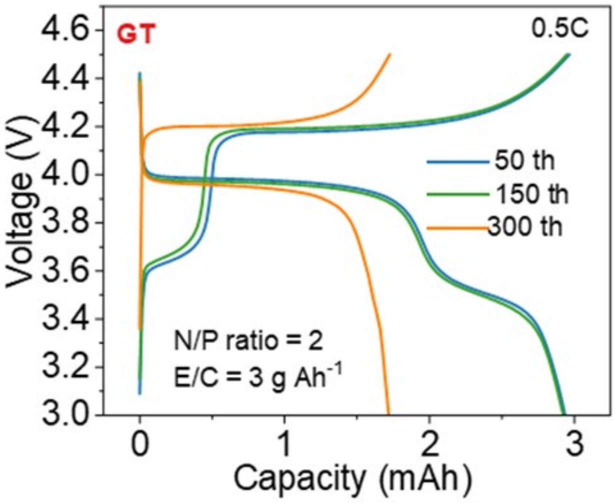

Figure S20. Voltage-capacity curves for the 50th, 150th and 300th cycles of Li|| LMFP with high N/P ratio in GT electrolyte.

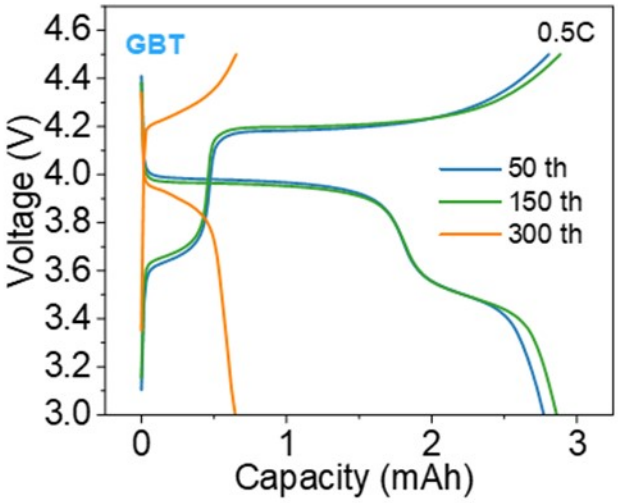

Figure S21. Voltage-capacity curves for the 50th, 150th and 300th cycles of Li|| LMFP with high N/P ratio in GBT electrolyte.

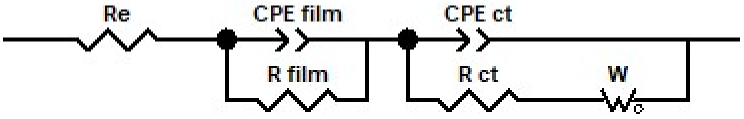

Figure S22. EIS datas are fitted to an equivalent electrical circuit model.

Table S3. Comparison of the electrochemical performance of recently reported lithium metal batteries with high-voltage cathodes (≥ 4.3 V).

Cathode	Li anode	Electrolytes	Voltage (V vs. Li$^+$/Li)	Capacity retention (%) / cycles	Reference
LM8F2P (5.4 mg cm^{-2}, 0.7 mAh cm^{-2})	250μm	EC-based electrolyte with 5% TFEC	3 - 4.5	62.5%, 800 cycles (1 C)	18
NCM523 (5 mg cm^{-2}, 1 mAh cm^{-2})	1 mm	Dual-Salt DHCE with 10 wt% FEC	3 - 4.6	89%, 200 cycles (1 C)	19
NCM523 (9.4 mg cm^{-2}, 1.76 mAh cm^{-2})	450μm	Ether-based DHCE	3 - 4.6	80.6%, 250 cycles (0.3 C)	20
NCM523 (19.7mg cm^{-2}, 3.54 mAh cm^{-2})	~50μm N/P=2		3 - 4.6	94%,100cycles (0.3 C)	
NCM811 (7.5 mg cm^{-2}, 1.5 mAh cm^{-2})	450μm	Ether-based DHCE	2.8 - 4.4	90%,300cycles (0.3 C)	21
NCM811 (20.47 mg cm^{-2}, 4.8 mAh cm^{-2})	50μm N/P=2	Ether-based DHCE	2.8 - 4.4	80%,120cycles (0.8/1.3 mA cm^{-2})	22
NCM811 (4.9 mAh cm^{-2})	50μm	Fluorinated-ether electrolyte	2.8 - 4.4	80%,270cycles (0.1 C/0.3 C)	23
LCO (2.2 mAh cm^{-2})	20μm N/P=1.8	Sulfone-based electrolyte	3 - 4.5	80%, 300cycles (0.2 C/1 C)	24
NCM811 (2.8 mAh cm^{-2})	20μm N/P=1.5		2.8 - 4.6	80%,180cycles (0.2 C/1 C)	
NCM811 (~7 mg cm^{-2}, ~1.3 mAh cm^{-2})	excess Li	Solid polymer electrolytes	2.8 - 4.5	80%,400 cycles (0.5 C)	25
LCO (2.5 mg cm^{-2}, 0.5 mAh cm^{-2})	excess Li	EC-based electrolyte with 2% FEC and	3 - 4.6	65.5%,1500 cycles (1 C)	26
			3 - 4.7	58.6%,600 cycles	

		VC		(1 C)	
NCM811 (9 mg cm^{-2}, 1.9 mAh cm^{-2})	450μm	LiFSI-DBE/TFMH	2.8 – 4.4	91.3%, 400 cycles (1 C)	27
NCM811 (21 mg cm^{-2} , 4.2 mAh cm^{-2})	50μm		2.8 – 4.4	95.6%,160 cycles (0.1 C/0.4 C)	
NCM811 (2 mg cm^{-2}, 0.35 mAh cm^{-2})	50μm	Polyphosphoester-based electrolyte	3 – 4.3	85.49%, 250 cycles (0.5 C)	28
LFP (2 mg cm^{-2}, 0.25 mAh cm^{-2})	50μm		2.5 – 4	91.28%,1000 cycles (1 C)	
NCM811 (1.52 mg cm^{-2} , 0.225 mAh cm^{-2})	excess Li	Aliphatic ketone-based solid polymer electrolyte	3 – 4.3	70%,250 cycles (0.1 C)	29
LFP (2.3 mg cm^{-2}, 0.391 mAh cm^{-2})			2.5 – 4	96%,700 cycles (0.5 C)	
LMFP (2 mg cm^{-2}, 0.262 mAh cm^{-2})			2.5 – 4.4	91%,200 cycles (0.2 C)	
LM8F2P (3.4 mg cm^{-2}, 0.5 mAh cm^{-2})	**250μm**	**Ether-based DHCE with 1% MPN**	**3 – 4.5**	**86.4%, 1400 (0.5C)**	**This work**
LM8F2P (19.5 mg cm^{-2}, 2.6 mAh cm^{-2})	**~ 20μm N/P=2**		**3 – 4.5**	**94%, 270 (0.5C)**	

LM8F2P: $LiMn_{0.8}Fe_{0.2}PO_4$; LFP: $LiFePO_4$; LCO: $LiCoO_2$; NCM811: $LiNi_{0.8}Co_{0.1}Mn_{0.1}O_2$; NCM523: $LiNi_{0.5}Co_{0.2}Mn_{0.3}O_2$; DHCE: Diluted high-concentration electrolyte.

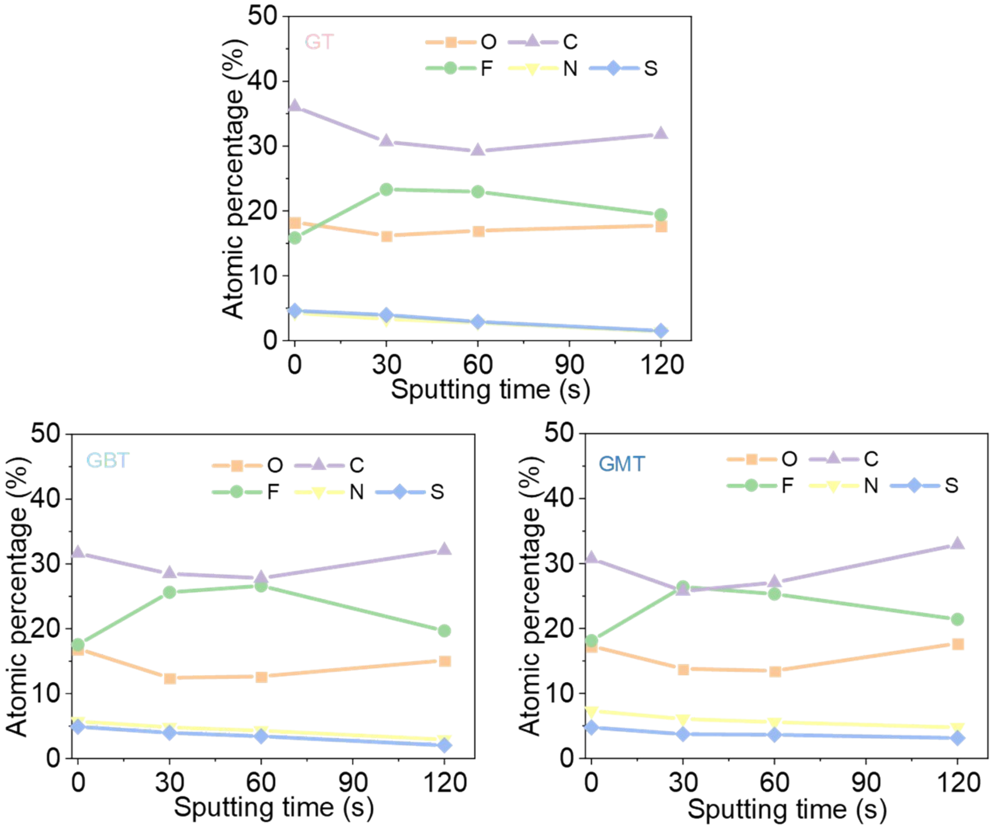

Figure S23. Elemental ratios for the CEIs on the cycled LMFP cathodes cathode after various etching time.

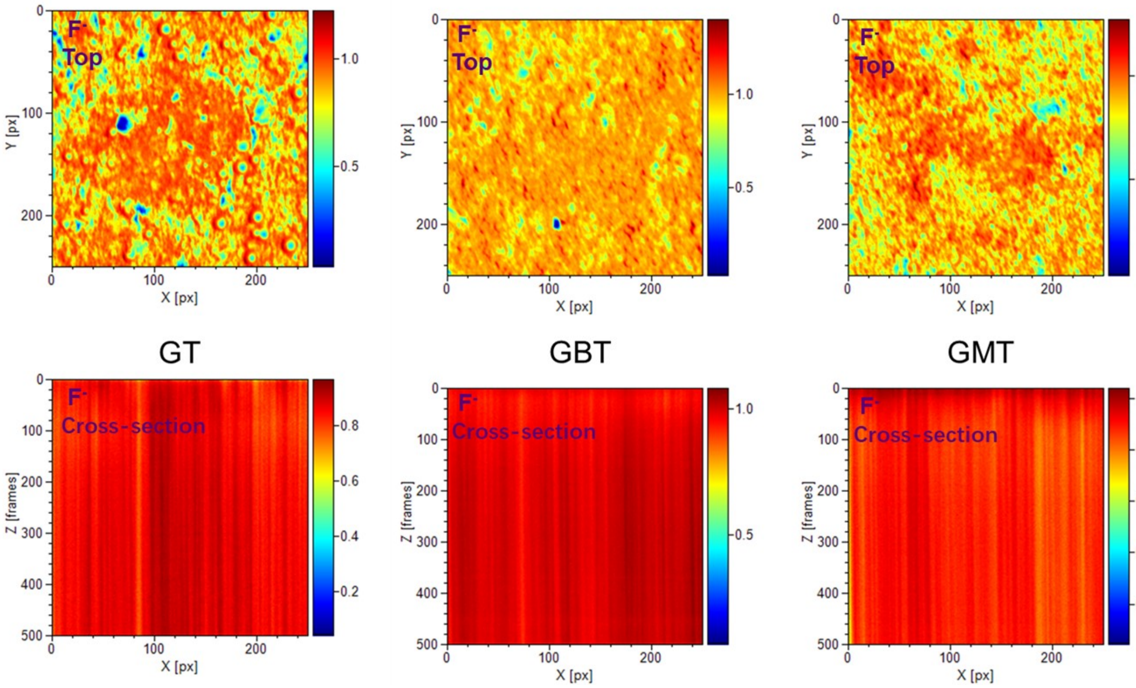

Figure S24. The top view and the cross-section view of F^- fragment for cycled LMFP cathode using different electrolytes.

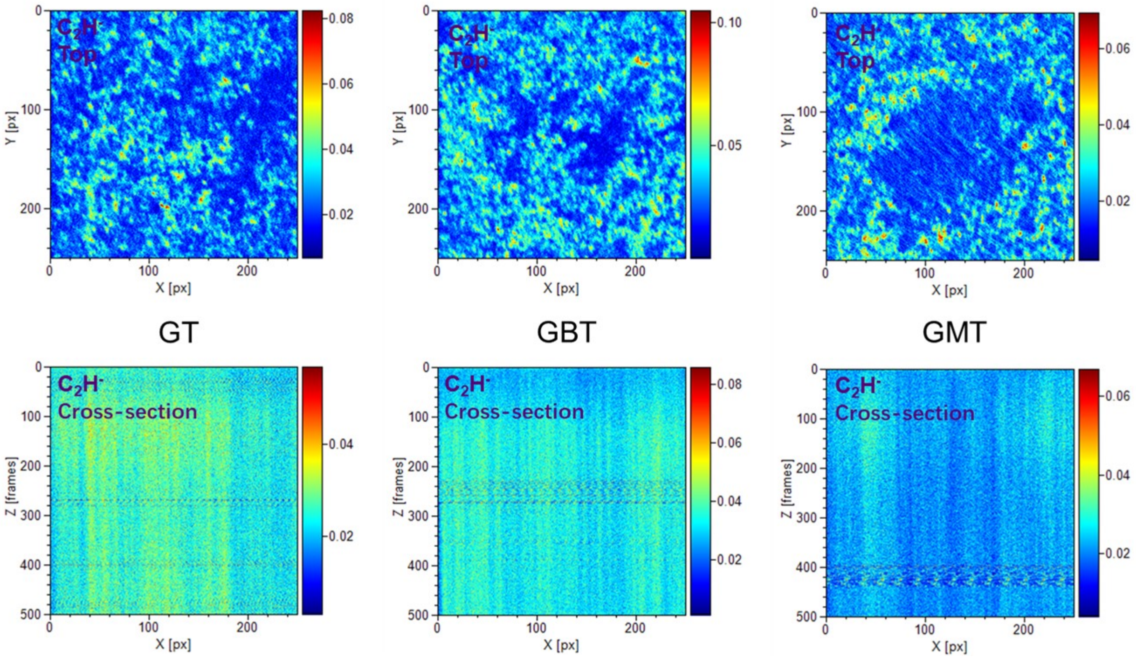

Figure S25. The top view and the cross-section view of C_2H^- fragment for cycled LMFP cathode using different electrolytes.

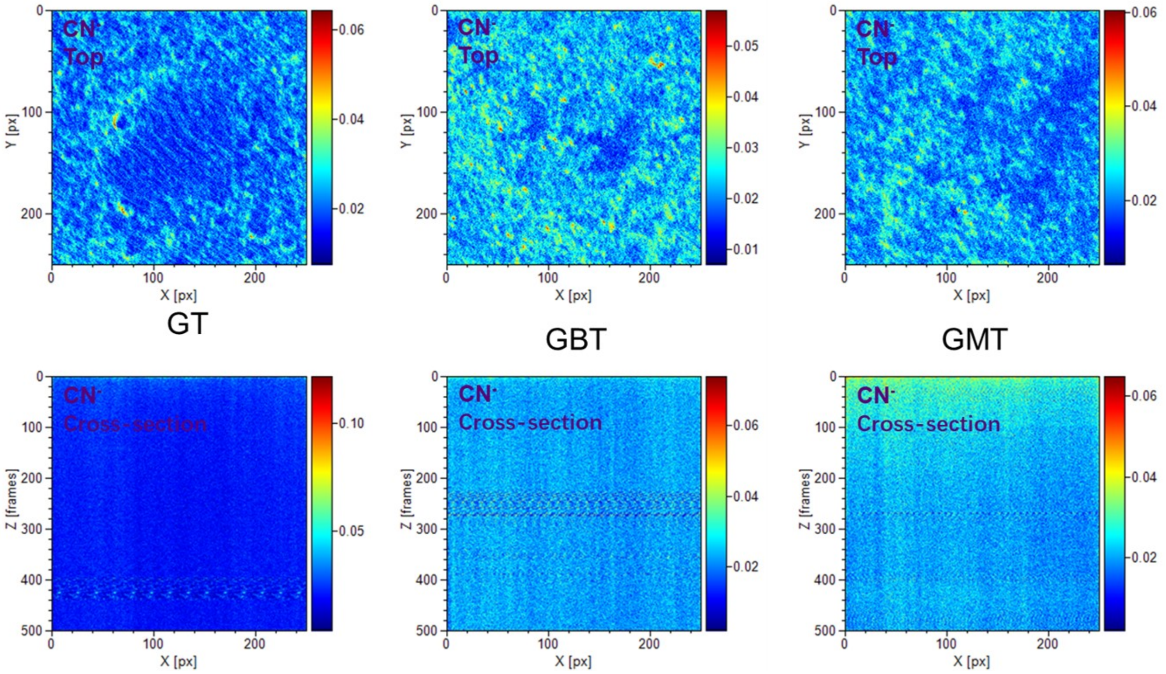

Figure S26. The top view and the cross-section view of CN^- fragment for cycled LMFP cathode using different electrolytes.

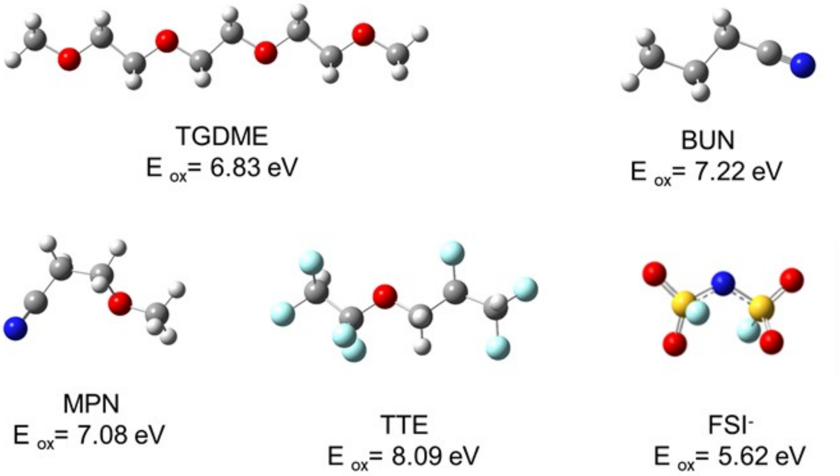

Figure S27. The calculated oxidation potentials (E_{ox}) of various individual species by DFT.

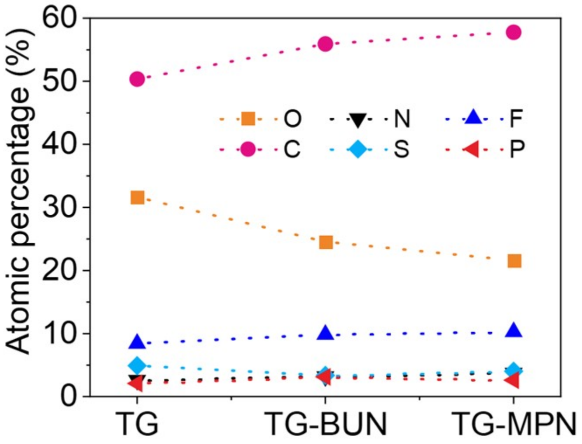

Figure S28. Quantified elemental atomic ratios of the CEI layer formed on cathodes in different electrolytes (after only two 0.1C formation cycles).

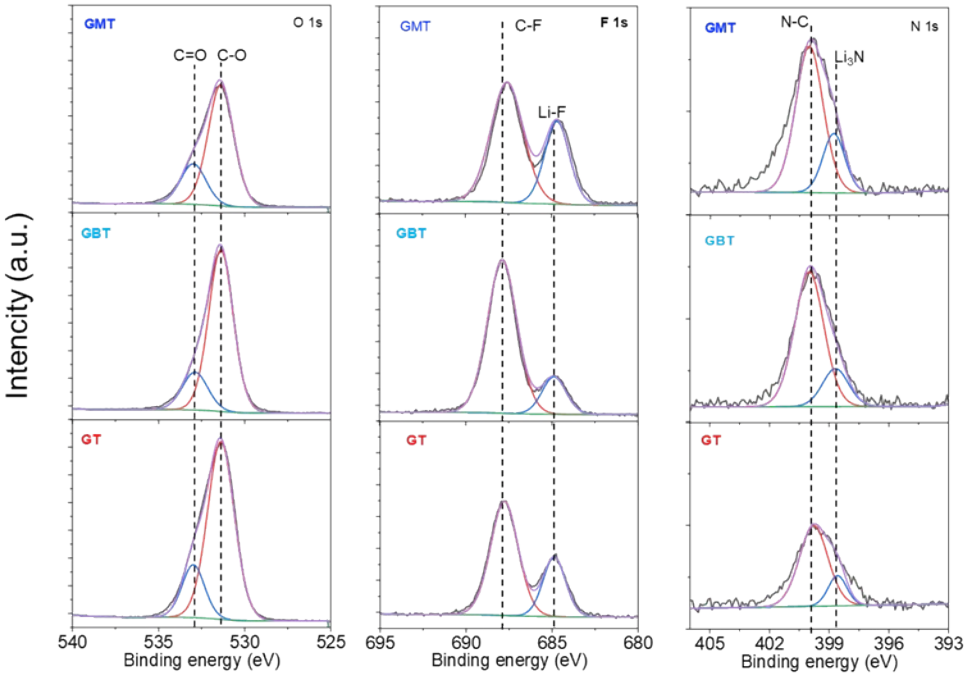

Figure S29. High-resolution XPS spectra showing the O 1s, N 1s, and F 1s core levels for the CEI formed on cathodes in different electrolytes (after only two 0.1C formation cycles).

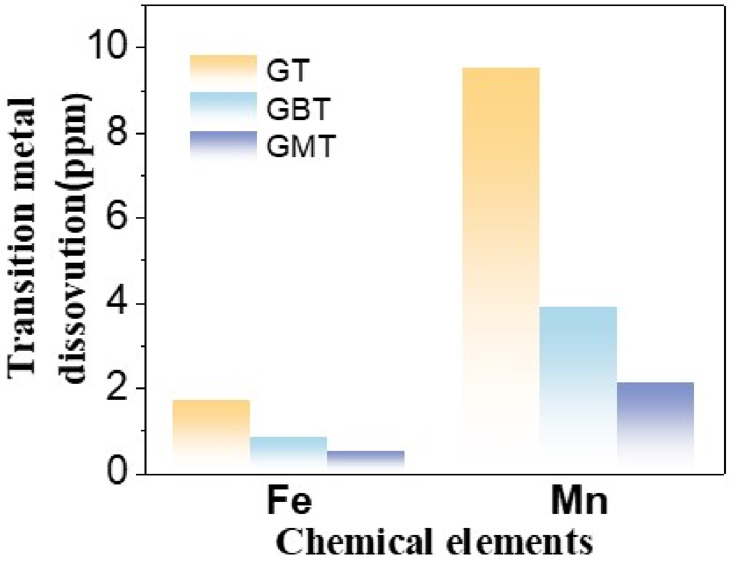

Figure S30. Transition metal dissolution tests by ICP.

Reference

[1] W. Chen, Q.Y. Luo, and H.S. Fang, Physical Chemistry Chemical Physics 2022, 24, 46, 28599-28608.

[2] Y.G. Zou, G. Liu, Y.Q. Wang, Q. Li, Z. Ma, D.M. Yin, Y. Liang, Z. Cao, L. Cavallo, H. Kim, L.M. Wang, H.N. Alshareef, Y.K. Sun, J. Ming, Advanced Energy Materials 2023, 13,19.

[3] B.D. Adams, J.M. Zheng, X.D. Ren, W. Xu, and J.G. Zhang, 8 ,7, 1702097, (2018).

[4] G. Kresse and J. Furthmuller, Phys. Rev. B 54, 11169, (1996).

[5] P. E. Blochl, ¨ Phys. Rev. B 50, 17953, (1994).

[6] J. P. Perdew, K. Burke, and M. Ernzerhof, Phys. Rev. Lett. 77, 3865, (1996).

[7] M. Frisch, G. Trucks, H. Schlegel, G. Scuseria, M. Robb, J. Cheeseman, G. Scalmani, V. Barone, G. Petersson, H. J. G. Nakatsuji, (2016).

[8] F. Weigend, R. J. P. C. C. P. Ahlrichs, Phys. Chem. Chem. Phys. 2005, 7, 3297.

[9] K. J. T. C. A. Raghavachari, Theor. Chem. Acc. 103, 361, (2000).

[10] M. J. Abraham, T. Murtola, R. Schulz, S. Páll, J. C. Smith, B. Hess, E. J. S. Lindahl, SoftwareX 1, 19, (2015).

[11]K. P. Jensen and W. L. Jorgensen, Journal of Chemical Theory and

Computation, 2, 6, 1499-1509, (2006).

[12]S. V. Sambasivarao, Journal of Chemical Theory and Computation, (2009).

[13] W. Humphrey, A. Dalke, K. J. J. o. m. g. Schulten, J. Mol. Graphics 14, 33, (1996).

[14] K. Momma, F. J. A. C. Izumi, J. Appl. Crystallogr. 44, 1272, (2011).

[15] X. Zhang et al., Adv. Energy Materials, 10, 22, (2020).

[16] L. Martinez, R. Andrade, E. G. Birgin, and J. M. Martinez, J Comput. Chem., 30, 2157-2164, (2009).

[17] X. Chen, X.-Q. Zhang, H.-R. Li, and Q. Zhang, Batteries & Supercaps, 2, 128-131, (2019).

[18] G. Fang, Y. Liu, Y. Feng, Y. Pan, H. Yang, Y. Liu, M. Wu, Chinese Chemical Letters 2025, 36(1):579-584.

[19]S. S. Lin, H. M. Hua, P. B. Lai, J. B. Zhao, Advanced Energy Materials 2021, 11 (36), 2101775.

[20]G. L. Hu, Z. L. Yang, X. X. Zhang, Y. C. Liu, Y. S. Lin, S. J. Chen, Y. Q. Chen, B. Sa, Y. N. Zhang, Energy Storage Materials 2024, 69, 103402.

[21]X. D. Ren, P. Y. Gao, L. F. Zou, S. H. Jiao, X. Cao, X. H. Zhang, H. Jia, M. H. Engelhard, B. E. Matthews, H. P. Wu, H. Lee, C. J. Niu, C. M. Wang, B. W. Arey, J. Xiao, J. Liu, J. G. Zhang, W. Xu, Proceedings of the National Academy of Sciences of the United States of America 2020, 117, 28603-28613.

[22]Y. L. Chen, Z. Yu, P. Rudnicki, H. X. Gong, Z. J. Huang, S. C. Kim, J. C. Lai, X. Kong, J. Qin, Y. Cui, Z. N. Bao, Journal of the American Chemical Society 2021, 143, 18703-18713.

[23]Z. Yu, P. E. Rudnicki, Z. W. Zhang, Z. J. Huang, H. Celik, S. T. Oyakhire, Y. L. Chen, X. Kong, S. C. Kim, X. Xiao, H. S. Wang, Y. Zheng, G. A. Kamat, M. S. Kim, S. F. Bent, J. Qin, Y. Cui, Z. N. Bao, Nature Energy 2022, 7, 94-106.

[24]W. Yang, J. Cai, C. Xu, A. Chen, Y. Wang, Y. Shi, P. He, H. Zhou, Advanced materials 2025, 37(34), 2505285.

[25]W. R. Zhang, V. Koverga, S. F. Liu, J. G. Zhou, J. Wang, P. X. Bai, S. Tan, N. K. Dandu, Z. Y. Wang, F. Chen, J. L. Xia, H. L. Wan, X. Y. Zhang, H. C. Yang, B. L. Lucht, A. M. Li, X. Q. Yang, E. Y. Hu, S. R. Raghavan, A. T. Ngo, C. S. Wang, Nature Energy 2024, 9, 386-400.

[26] X. Li, X. Zhu, Y. Zhang, L. Han, J. Gao, D. Liu, J. Qiu, W. Zhou, Advanced materials 2025, 37(35), 2506228.

[27] F. Hai, Y. Ban, W. Xue, Y. Yang, W. Yan, W. Hua, W. Tang and M. Li, Advanced Functional Materials, 2025, 36(4), 2514536.

[28] Y. Wang, Z. Chen, H. Zhang, F. Tian, J. Wang, Y. Zhu, G. Yang, Z. Li, G. Cui, Advanced Materials, 2025, 38(3), 2514210.

[29] Y. Jiang, B. Wujieti, Y. Liu, Q. Zeng, Z. Li, J. Guan, H. Wang, L. Chen, Y. Cao, R. Li, Y. Zhou, H. Zhou, W. Cui, and L. Zhang, Advanced Functional Materials, 2024, 35(19), 2421160.